Volcano deformation and eruption forecasting

Paul Segall

Geological Society, London, Special Publications v.380, first published March 20, 2013; doi 10.1144/SP380.4

Notes

Geological Society, London, Special Publications published online March 20, 2013 as doi: 10.1144/SP380.4

Volcano deformation and eruption forecasting

PAUL SEGALL

Department of Geophysics, Stanford University, Stanford, CA 94305-2115, USA (e-mail: segall@stanford.edu)

Abstract: Recent advances in Global Positioning System (GPS), tilt and Interferometric Synthetic Aperture Radar (InSAR) have greatly increased the availability of volcano deformation data. These measurements, combined with appropriate source models, can be used to estimate magma chamber depth, and to provide information on chamber shape and volume change. However, kinematic models cannot constrain magma chamber volume, and provide no predictive capability.

Volcanic eruptions are commonly preceded by periods of inflation. Under appropriate conditions, eruptions are 'inflation predictable'; that is, subsequent eruptions occur when inflation recovers the deflation during the preceding event. Notable successes in forecasting eruptions have come largely through the ability to discern repeatable patterns in seismic activity, ground deformation and gas emission, combined with historical and geological evidence of past eruptive behaviour. To move beyond empirical pattern recognition to forecasting based on deterministic physical–chemical models of the underlying dynamics, will require integration of different data types and models. I suggest two areas poised for progress: quantitative integration of deformation and seismicity; and model-based forecasts conditioned on estimates of material parameters and initial conditions from inversion of available datasets.

Deformation and seismicity are the principal geophysical methods for volcano monitoring, and in some cases have signalled dyke propagation minutes to hours prior to eruptions. Quantitative models relating these processes, however, have been lacking. Modern theories of seismicity rate variations under changing stress conditions can be used to integrate deformation and (volcano–tectonic) seismicity into self-consistent inversions for the spatio-temporal evolution of dyke geometry and excess magma pressure. This approach should lead to improved resolution over existing methods and, perhaps, to improved real-time forecasts.

The past few decades have also witnessed a marked increase in the sophistication of physical–chemical models of volcanic eruptions. I review conduit models that can be combined with GPS and extrusion rate data through Markov Chain Monte Carlo (MCMC) inversion to estimate the absolute volume of the crustal magma chamber, initial chamber overpressure, initial volatile concentrations and other parameters of interest. The MCMC estimation procedure can be extended to deterministic forecasting by using the distribution of initial conditions and material parameters consistent with available data to initiate predictive forward models. Such physics-based MCMC forecasts would be based on all knowledge of the system, including data up to the current date. The underlying model is completely deterministic; however, because the method samples initial conditions and physical parameters consistent with the given data, it yields probabilistic forecasts including uncertainties in the underlying parameters. Because there are almost certain to be effects not factored into the forward models, there is likely to be a substantial learning curve as models evolve to become more realistic.

As magma is transported through the crust, it generally deforms the Earth's surface in ways that can be measured by both terrestrial and spaceborne sensors. In the brittle–elastic crust, these strains are usually associated with volcano–tectonic (VT) earthquakes. For these reasons, deformation and seismicity are the principal geophysical methods for monitoring volcanoes, and provide important constraints on subsurface magma chambers and conduits.

The past decades have witnessed tremendous growth in continuous GPS networks and improvements in Interferometric Synthetic Aperture Radar (InSAR) imaging, such that for an increasing number of volcanoes we have both continuous and spatially extensive datasets. Global Positioning System (GPS) receivers are now commonly deployed in continuous operational mode, returning high-precision three-dimensional displacement data in (some cases) near real time. InSAR-capable satellites routinely image active volcanoes, returning spatially dense images of ground displacement. As the number of InSAR satellites has increased, the sampling interval has decreased to, in some cases, several days between image acquisitions. At the same time, ever more volcanoes have some seismic monitoring, and the better-instrumented volcanoes contain broadband seismometers capable of

From: PYLE, D. M., MATHER, T. A. & BIGGS, J. (eds) *Remote Sensing of Volcanoes and Volcanic Processes: Integrating Observation and Modelling*. Geological Society, London, Special Publications, **380**, http://dx.doi.org/10.1144/SP380.4

revealing detailed source information. My focus in this paper will be on geophysical methods, although important advances in gas measurement systems have also contributed significantly to improved volcano monitoring.

Deformation measurements have traditionally been analysed using geometrically simple kinematic sources in elastic half-spaces. The data are sensitive to source depth and shape, and to changes in volume, rather than total magma volume. Inferences of pressure change depend on elastic constants as well as (often difficult to constrain) dimensions of the magma body. In addition, dyke intrusions generate characteristic deformation patterns, and are commonly associated with propagating earthquake swarms, making them relatively easy to identify.

There have been a number of successful eruption forecasts. These have been largely empirical, constrained by both geophysical and gas emission data, past eruptive behaviour (historical and geological), and practical experience at similar volcanoes. In the past few years, researchers have also developed increasingly sophisticated physical and thermodynamic models of volcanic systems. I suggest that the combination of more realistic models and vastly improved datasets warrant consideration of a deterministic approach to eruption forecasting. In order to move beyond kinematic descriptions and explicitly relate geophysical observations to the absolute (rather than relative) properties of magma reservoirs and conduits, it is necessary to integrate fluid-dynamical models of volcanic processes into the analysis of deformation. These are not new ideas. Previously, Sparks (2003) wrote 'Forecasting is evolving from empirical pattern recognition to forecasting based on models of the underlying dynamics' (p. 1). He also noted that 'Flow models will need to be coupled into models of edifice deformation' (Sparks 2003, p. 10).

I will attempt here to outline fruitful approaches to this problem. We focus not only on the problem of anticipating the onset of an eruption but, also, on whether once an eruption is underway we can bound its ultimate size and duration, a problem highlighted by the air traffic disruption caused by the 2010 Eyjafjallajökull eruption.

Volcano deformation

The monitoring of deformation on volcanoes, particularly basaltic shields in Hawaii and Iceland, has lead to recognition that volcanoes *inflate* as magma accumulates in crustal reservoirs, and then *deflate* as magma is withdrawn, either to erupt at the surface or to intrude into the surrounding crust. Short-term inflation–deflation cycles are well documented, associated, for example, with episodic high-fountaining eruptions during the early stages of the Pu'u O'o eruption of Kilauea Volcano. Longer-term inflation has been documented prior to many, but not all, eruptions at a variety of volcanoes around the world (see the subsection on 'Inflation predictable eruptions?' later). For example, inflation was *not* detected prior to the 2004–2008 dome-forming eruption of Mount St Helens (Lisowski *et al.* 2008). However, some silicic calderas have experienced rapid uplift, without (yet) erupting (e.g. Campi Flegrei, Long Valley: Dvorak & Dzurisin 1997).

Volcano deformation data has traditionally been interpreted in terms of rather idealized kinematic models. For example, displacements on the Earth's surface resulting from a pressure change, Δp, in an ellipsoidal magma chamber with semi-axes $a \geq b \geq c$, in the limit that the magma chamber depth, d, is substantially larger than the chamber dimensions, can be written as:

$$u_i = \frac{\Delta p V_0}{\mu d^2} f_i\left(\frac{r}{d}, \frac{a}{b}, \frac{a}{c}, \nu\right) \tag{1}$$

where V_0 is the volume of the magma chamber, d is the depth to the chamber centroid and μ is the elastic shear modulus. The function f_i depends on the component of displacement (vertical or radial in the case of axisymmetric chambers), the normalized distance from the chamber, r/d, the aspect ratios a/b, a/c, and the Poisson's ratio, ν (details are given in Yang *et al.* 1988 and Segall 2010, chap. 7). Equation (1) is specialized for the case where one principal axis is vertical; for dipping chambers f_i also depends on the dip angle and direction. The simplest, and most widely used, case is the approximation to a spherical magma chamber of radius a, in the limit that $a/d \ll 1$; the so-called Mogi source (Mogi 1958; McTigue 1987). In this case f_i becomes:

$$f_i\left(\frac{r}{d}, \nu\right) = \frac{3(1-\nu)}{4\pi} \frac{\xi_i}{\left[\left(\frac{r}{d}\right)^2 + 1\right]^{3/2}} \tag{2}$$

where for vertical displacement $\xi_z = 1$, while for radial displacement $\xi_r = r/d$. It is clear from Equation (1) that deformation data normally cannot determine the size of the magma chamber (V_0) nor the pressure change independently. For a spherical magma chamber, the change in volume is $\Delta V = \pi \Delta p a^3/\mu$, so that the magnitude of the deformation signal is proportional to the subsurface *volume change*, ΔV. The depth of the magma chamber can be estimated from the distance scale over which the vertical displacement decays from the peak, as in Equation (2).

The ratio of vertical to horizontal displacement can be used to determine general aspects of the magma chamber shape (Dieterich & Decker 1975; Segall 2010). Vertically elongate, stock-like chambers generate larger horizontal displacement relative to the vertical, while sills are efficient at generating vertical deformation.

In summary, conventional interpretation of deformation data through kinematic models allows for estimation of: (1) the magma chamber depth (from the distance scale over which deformation decays with distance); (2) limited information about chamber geometry (from the ratio of horizontal to vertical deformation); (3) source strength, ΔpV_0, or volume change, ΔV (from the amplitude of the deformation signal); and (4) potentially, some information about orientation for non-radially symmetric sources, particularly dykes. These models, combined with extensive InSAR and GPS data, have led to important insights into the subsurface plumbing of magmatic systems.

Examples

In this subsection we briefly review just a few of the more striking examples of volcano deformation observed from GPS and InSAR.

A remarkable set of observations has been obtained for Sierra Negra Volcano in the Galapagos from a combination of InSAR (Fig. 1) and GPS measurements. The first insights came from InSAR, which revealed that the caldera floor uplifted during the 1990s at rates of between 32 (1992–1997) and 65 cm a^{-1} (1998–1999) (Amelung *et al.* 2000). Subsequent interferograms exhibited the same characteristic deformation pattern (as in Fig. 1a, c), at varying rates, over the last decade, punctuated by episodes of faulting and eruption (Chadwick *et al.* 2006). The stable deformation pattern reflects the fixed magma chamber geometry. By examining the ratio of vertical to horizontal deformation from ascending and descending InSAR tracks, Yun *et al.* (2006) showed that the deformation is induced by a sill-like structure roughly 2 km beneath the caldera floor. Specifically, the InSAR data can be well explained by a uniformly pressurized horizontal crack, slightly oblong in shape. It should be noted, however, that thin sills and flat-topped diapirs produce nearly identical surface deformation when the depth to the top of the magma body is less than the chamber radius (Yun *et al.* 2006). In this limit, the deformation is determined solely by the displacement of the upper chamber surface; the sides and bottom do not contribute. The data thus cannot distinguish between a thin sill and a larger roughly flat-topped chamber. Thermal considerations, however, do place constraints on the thickness of the chamber such that it remains largely fluid over decadal timescales.

The more surprising observation (Fig. 1b) was the very asymmetric uplift pattern with a phase discontinuity across a previously identified intracaldera fault. From the interferometry, it was inferred that there was approximately 80 cm of throw on the fault (Amelung *et al.* 2000), apparently associated with a M_w 5.0 earthquake. The seismic moment, however, was too small to account for the observed deformation, suggesting that much of the slip was aseisimc. The 'trap-door' faulting was later confirmed by radar pixel offsets, which do not suffer from cycle skipping as in the interferometric phase (Jónsson *et al.* 2005). A second, similar trap-door faulting event took place in April 2005 associated with a M 4.6 earthquake (Chadwick *et al.* 2006) (Fig. 2), in which the southern caldera floor uplifted by 84 cm.

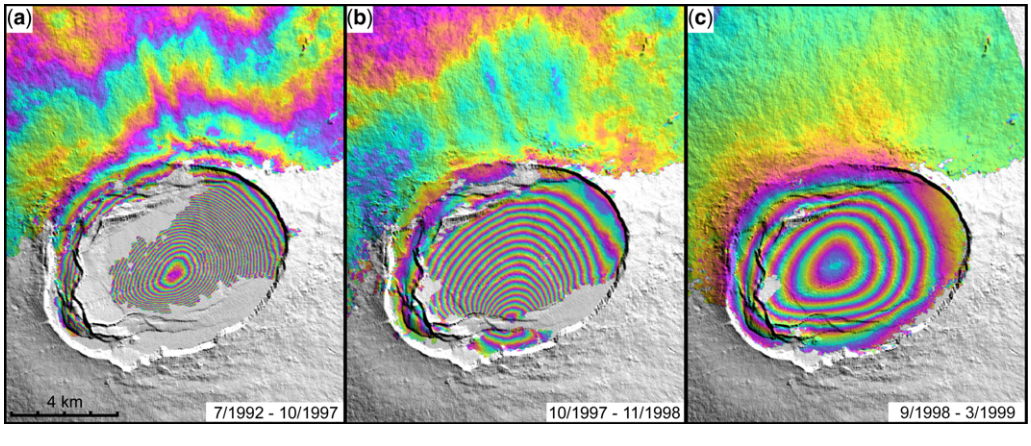

Fig. 1. Radar interferograms of Sierra Negra Volcano for: (**a**) 1992–1997; (**b**) 1997–1998; and (**c**) 1998–1999.

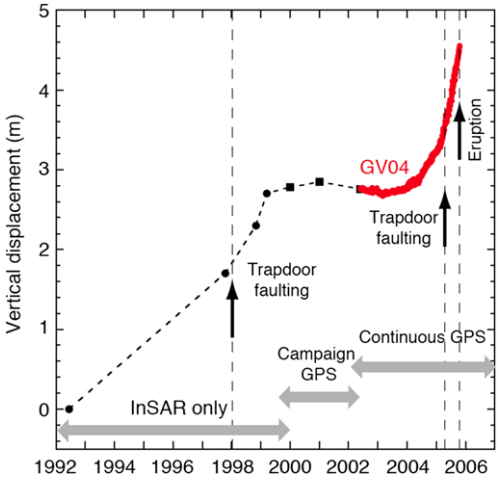

Fig. 2. Uplift of Sierra Negra from a combination of InSAR and GPS data. Isolated black dots indicate uplift from InSAR, continuous dots (red in online version) from continuous GPS receiver in the centre of the Caldera. Times of trapdoor faulting and 2005 eruption indicated. After Chadwick *et al.* 2006.

GPS measurements on Sierra Negra began in 2000 and by 2002 a six-station continuous network was deployed in the caldera. These data document a change from slight deflation to accelerating uplift beginning in 2003, ending with a fissure eruption on 22 October 2005 (Fig. 2). From the combined InSAR and GPS data, Chadwick *et al.* (2006) inferred nearly 5 m of uplift prior to the 2005 eruption. The eruption was preceded by a third trapdoor faulting event (M_w 5.5) about 3 h prior to the eruption on the SW segment of the intra-caldera fault – on the opposite side of the caldera from the eruptive fissures (Geist *et al.* 2008). The timing of the eruption so soon after the M_w 5.5 event strongly implies a causal connection; however, the physical connection has not been explained. Interestingly, the April trapdoor faulting episode, only 4 months earlier, did not trigger the eruption and, indeed, did not apparently perturb the rate of inflation. The eruption lasted 8 days, extruding 150×10^6 m^3 of basalt, leading to roughly 5 m of subsidence of the caldera floor.

Another striking example of volcano deformation discovered by InSAR was the dramatic rifting episode on the Dabbahu segment of the Afar Rift in Ethiopia, beginning in September of 2005 (Wright *et al.* 2006). The September 2005 dyke injection, accompanied by a strong earthquake swarm, was imaged with Envisat satellite data. Analysis of these data suggests a roughly 60 km-long dyke, extending from 2 to 9 km depth, and opening by as much as 8 m (Wright *et al.* 2006; Grandin *et al.* 2009). Estimated dyke volumes range from 1.5 to 2.5 km^3, making it the largest dyke intrusion detected geodetically. The dyking event was associated with substantial slip on graben-bounding faults above the dyke, visible both in the field and in InSAR imagery.

As was the case during the Krafla, Iceland fissure swarm beginning in the late 1970s, the giant 2005 Dabbahu dyke was followed by a sequence of smaller intrusions (Ebinger *et al.* 2010). There have been 14 subsequent intrusions between 2006 and 2010 (Wright *et al.* 2012), tending to fill in areas with less opening during the initial event (Fig. 3). Volumes of the later dykes range from 0.04 to 0.17 km^3 (Ebinger *et al.* 2010).

InSAR observations provide synoptic information that can reveal previously unforeseen processes. Continuously recording systems, including permanent GPS, tiltmeters and strainmeters, provide tighter constraints on the temporal evolution of intrusions and eruptions, which can be vital in eruption forecasting.

The 1997 East Rift Zone (Napau) intrusion and eruption on Kilauea Volcano, Hawaii occurred as

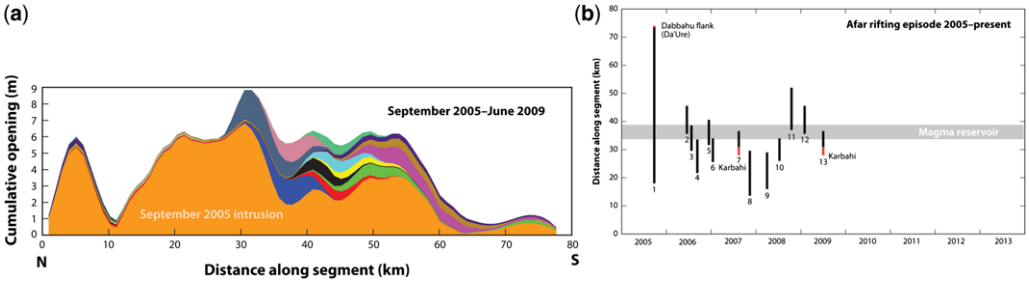

Fig. 3. (**a**) Depth-averaged dyke opening for the Dabbahu dyke swarm v. distance along the rift axis. Colours represent different intrusions. (**b**) Space–time pattern of dykes for intrusions up to 2009, red indicates eruption. From Ebinger *et al.* (2010).

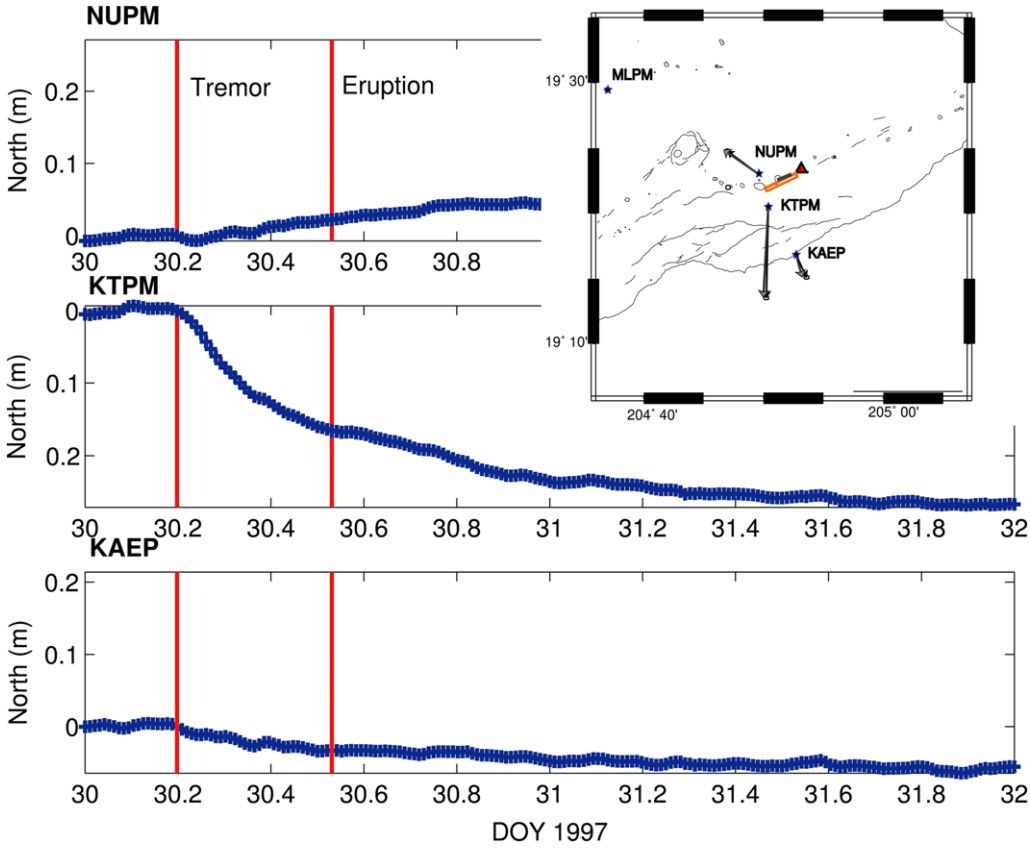

Fig. 4. North component of GPS time series at three stations during the 1997 Napau dyke intrusion and eruption on Kilauea volcano. Time is Day of Year (DOY) in 1997. First vertical line marks the onset of volcanic tremor, the second the onset of the eruption. Inset shows station locations; MLPM on Mauna Loa was used as a reference station in the GPS analysis. Best-fitting uniform opening dislocation to all of the GPS data (Owen *et al.* 2000) is shown as the rectangle (orange in online version) in the inset map.

the continuous GPS network there was being installed. At that time, there were three continuous GPS sites in the vicinity of the eruptive fissures. Time series of the GPS North component of displacement are shown in Figure 4. As expected, NUPM north of the dyke displaced to the north, while the other two stations displaced to the south. The best-fitting dislocation model of the intrusion (including campaign GPS data) aligns well with the eruptive fissures, and the decay in displacement with distance from the dyke constrains the bottom of the dyke to about 2.5 km (Owen *et al.* 2000). The displacements began, coincident with the onset of volcanic tremor, roughly 8 h prior to the dyke breaching the surface and the eruption onset. These and other data indicate that deformation and seismic data can provide societally useful warnings of eruptions in some basaltic volcanoes, as discussed more in the section on 'Eruption forecasting' later.

Physics-based eruption models

As mentioned at the start of this paper, the past few decades have witnessed a marked increase in the sophistication of physical–chemical models of volcanic eruptions (Wilson *et al.* 1980; Stasiuk *et al.* 1993; Woods 1995; Mastin & Ghiorso 2000; Dobran 2001; Huppert & Woods 2002; Sahagian 2005). Such models include the changes in physical properties (density, viscosity and compressibility) as pressure decreases and volatiles exsolve from the melt phase. Some studies include the effects of crystallization, possibly including kinetics, as well as gas loss to the surrounding wall rocks (Melnik & Sparks 2005; Collombet 2009; Kozono & Koyaguchi 2009). Many of these analyses consider the flow of magma in rigid cylindrical or dyke-like conduits, without consideration of coupling to the elastic surroundings. More recently, a number of studies

have included the influence of shear and normal tractions acting on the walls of the conduit on the deformation of the surrounding rocks. Including this fluid–solid coupling allows the effects of magma flow through the conduit to be compared to measured surface deformations and, perhaps, seismicity (Collier & Neuberg 2006; Nishimura 2009; Albino *et al.* 2011). This possibility allows one to connect fundamental flow processes to geophysical observables.

I first review closed-forms solutions for a deflating elastic magma chamber, with constant physical properties, and then briefly discuss numerical solutions through a conduit with pressure-dependent properties. Finally, I discuss how the predictions of these models can be compared to deformation and other observables.

Linearizing the mass change within the magma chamber, $\mathrm{d}m/\mathrm{d}t = \mathrm{d}(\rho V)/\mathrm{d}t = \rho_0 \mathrm{d}V/\mathrm{d}t + V_0 \mathrm{d}\rho/\mathrm{d}t$, and defining the magma and magma-chamber compressibilities as $\beta_\mathrm{m} = (1/\rho)\partial\rho/\partial p$ and $\beta_\mathrm{ch} = (1/V)\partial V/\partial p$ leads to:

$$\frac{\mathrm{d}p_\mathrm{ch}}{\mathrm{d}t} = \frac{q_\mathrm{in} - q_\mathrm{out}}{\rho_0 V_0 \bar{\beta}} \qquad \bar{\beta} = (\beta_\mathrm{m} + \beta_\mathrm{ch}) \tag{3}$$

(Segall *et al.* 2001), where p_ch is the pressure within the magma chamber (taken at the centroid of the chamber), and q_in, q_out are the mass fluxes into and out of the magma chamber, respectively.

For a cylindrical conduit, the radial averaged momentum conservation equation can be written as:

$$0 = \rho g - \frac{\partial p}{\partial z} + \frac{8\eta v}{R^2} \tag{4}$$

where R is the conduit radius, η the viscosity and v the radially averaged velocity (Jaupart & Tait 1990). For a conduit of length L, we may approximate the vertical pressure gradient $\partial p/\partial z$ as p_ch/L. The mass flux through the conduit is $q_\mathrm{out} = \rho_0 \pi R^2 v$. From Equation (4), the flux is proportional to the difference between the chamber pressure and the magmastatic head, $\rho g L$:

$$q_\mathrm{out} = \frac{\pi \rho_0 R^4}{8\eta L}(p_\mathrm{ch} - \rho g L) \equiv \alpha \rho_0 (p_\mathrm{ch} - \rho g L) \tag{5}$$

Similarly, we assume that the flux into the chamber is proportional to the difference between the chamber pressure and that in a deep reservoir. Allowing the hydrostatic head between the deep reservoir and the chamber to be absorbed into the definition of p_deep:

$$q_\mathrm{in} = \rho_0 \Omega (p_\mathrm{deep} - p_\mathrm{ch}) \tag{6}$$

where Ω is a proportionality constant. Combining Equations (3), (5) and (6), yields a first-order equation for the chamber pressure:

$$\frac{\mathrm{d}p_\mathrm{ch}}{\mathrm{d}t} = \frac{\Omega(p_\mathrm{deep} - p_\mathrm{ch}) - \alpha(p_\mathrm{ch} - \rho g L)}{V_0 \bar{\beta}} \tag{7}$$

The solution to Equation (7) is given in Equation (8), along with an expression for the extruded volume, which is simply the integral (from $t = 0$ to $t = \infty$) of the volume flux, $V_\mathrm{ex} = \int q_\mathrm{out} \mathrm{d}t/\rho_0$,

$$\frac{p(t) - p_0}{p_0 - \rho g L} = -\left(\frac{\alpha}{\Omega + \alpha}\right)(1 - \mathrm{e}^{-t/t_\mathrm{c}}) \tag{8}$$

$$\frac{V_\mathrm{ex}(t)}{V_0 \bar{\beta}(p_0 - \rho g L)} = \left(\frac{\alpha}{\Omega + \alpha}\right) \times \left[\left(\frac{\alpha}{\Omega + \alpha}\right)(1 - \mathrm{e}^{-t/t_\mathrm{c}}) + \frac{t}{t_\mathrm{c}}\left(\frac{\Omega}{\Omega + \alpha}\right)\right] \tag{9}$$

where $t_\mathrm{c} \equiv V_0 \bar{\beta}/(\Omega + \alpha)$. This extends Huppert & Woods (2002) and Mastin *et al.* (2008) by including a pressure-dependent (rather than a time-invariant) recharge into the magma chamber. Results are illustrated in Figure 5. The excess pressure (over magmastatic) decays exponentially with time constant t_c. In the limit of no recharge and constant viscosity Newtonian flow, $t_\mathrm{c}(\Omega \to 0) = 8\eta V_0 \bar{\beta} L/\pi R^4$. The normalized excess pressure decays to $\alpha/(\Omega + \alpha)$, the steady-state pressure in which influx exactly balances outflow (see Equation 7). In the absence of recharge, the final pressure is simply the hydrostatic head $p(t \to \infty) = \rho g L$. In this same limit, the erupted flux decays exponentially, such that the final extruded volume is given by $V_0 \bar{\beta}(p_0 - \rho g L)$, the product of the chamber volume, excess pressure and the total compressibility. With recharge, the system evolves to steady-state outflux (linearly increasing extruded volume) balanced by inflow.

It is worth noting that this model, which does not include crystallization or other processes that could cause the eruption to cease, must tend towards one of two states: without influx, the chamber pressure decays to magmastatic and the eruption ends; with influx, the chamber pressure tends towards steady-state with equal fluxes into and out of the chamber, and the eruption continues indefinitely.

The estimation problem

As discussed in the section 'Volcano deformation', the spatial distribution of deformation can be used to constrain the depth and aspect ratio of the magma chamber. Given that information, and ignoring recharge, there are four additional unknowns

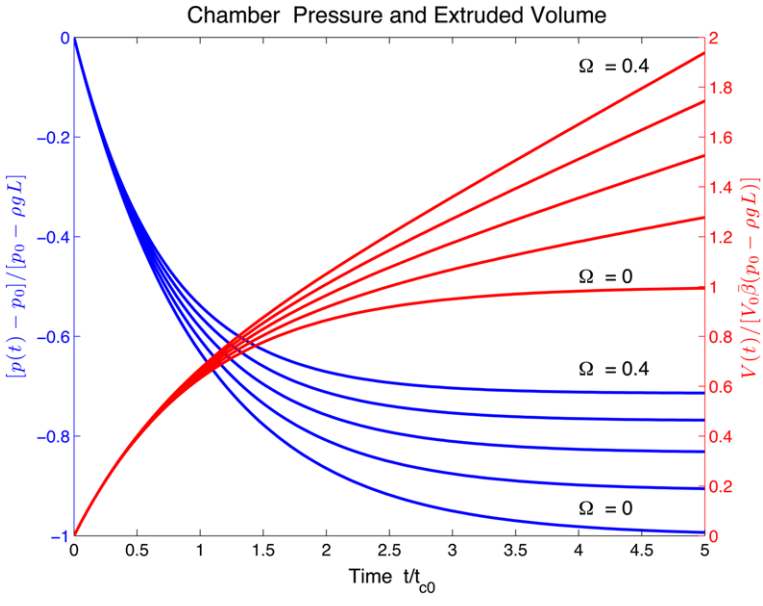

Fig. 5. Normalized pressure (left axis) and normalized extruded volume (right axis) as a function of t/t_c, from Equations (8) and Equation (9). Ω is the recharge parameter, defined by Equation (6). For $\Omega = 0$, there is no recharge into the magma chamber.

that would be very desirable to estimate: the initial magma chamber volume, V_0; the system compressibility, $\bar{\beta}$, which depends on volatile content and chamber geometry; the initial excess pressure, $\Delta p_0 = p_0 - \rho g L$; and the conduit flux parameter, α, which depends on conduit radius and magma viscosity (Equation 5). If the surface deformation is dominated by pressure change in the magma chamber – changing conduit tractions are likely only to effect stations very close to the vent – then, from Equations (8) and (9), there are only three independent observables as, with zero recharge, pressure change and extruded volume are scaled versions of one another: (1) the cumulative geodetic displacement (proportional to the final pressure change); (2) the final extruded volume; and (3) the time constant, t_c. Thus, there is generally one fewer observable than parameters to be estimated. Note that if the magma chamber geometry does not evolve with time, the space–time evolution of the deformation field is separable into a fixed spatial pattern multiplying a time-varying source strength.

Notice from Equation (3) that, without recharge, $(q_{out}/\rho_0)/\dot{p}_{ch} = -V_0\bar{\beta}$, where the overdot indicates time derivative and q_{out}/ρ_0 is the volume flux. This makes physical sense, in that the erupted flux per unit pressure drop is greater when the magma chamber volume and/or compressibility is large. From Equation (1), assuming that the chamber geometry does not vary with time, such that the velocity of a geodetic station at distance r, can be written as:

$$\dot{u}(r) = \frac{V_0\dot{p}}{\mu d^2} f\,(r/d, a/b, \ldots). \qquad (10)$$

Combining this with $(q_{out}/\rho_0)/\dot{p}_{ch} = -V_0\bar{\beta}$, yields:

$$\frac{q_{out}/\rho_0}{\dot{u}(r)d^2} f\,(r/d, a/b, \ldots) = \bar{\beta}\mu. \qquad (11)$$

Thus, the ratio of the volume flux to a normalized station velocity yields the scaled compressibility of the magmatic system $\bar{\beta}\mu$. If the shear modulus of the crust and the shape of the magma chamber can be reasonably well constrained, such measurements could place constraints on the exsolved volatile content of the magma. Similarly, if the magma compressibility increased during an eruption due to increased exsolution, buffering the pressure drop (Woods & Huppert 2003), this might be detected as an increase in the ratio of volume flux to station velocity.

If α were known independently, the magma chamber volume could be estimated from the characteristic decay time and compressibility, $V_0 = \alpha t_c/\bar{\beta}$. The initial overpressure could also be estimated from the initial erupted flux from Equation (5). Of course, α is dependent on the

conduit geometry and magma rheology. For Newtonian flow in cylindrical conduits, α is very sensitive to conduit radius. Nevertheless, it should be possible to put sensible bounds on this and other physical parameters. For example, if the initial magma chamber pressure is too large it would lead to fracturing of the conduit or chamber walls. For dome-forming eruptions, the initial magma pressure must be sufficient to raise the extruded dome above the vent (Mastin *et al.* 2009). Volatile content can often be bounded based on petrological observations. Because of strong correlations between parameters, bounds on some parameters may lead to tighter constraints on many other parameters, as discussed in Anderson & Segall (2013).

More realistic physics and Monte Carlo inversion

The simple model described in the previous subsection with constant physical properties does not account for the exsolution of dissolved volatile phases, and the concomitant changes in magma density, compressibility and melt viscosity (Mastin *et al.* 2008). The model can, however, be extended to include a multiphase magma consisting of liquid and crystals, as well as dissolved and exsolved volatile phases (Anderson & Segall 2011). In this study, the volatile solubility depends on pressure and composition (mole fraction of H_2O and CO_2) consistent with laboratory data, and the viscosity (assumed Newtonian) of the liquid phase increases as the dissolved water content decreases. At a fixed depth, the magma is assumed to crystallize forming a solid plug that displaces upwards along ring faults. Slip on the ring faults is governed by a rate-dependent friction law. The governing equations of momentum and mass balance are radially averaged, and the resulting system of equations is solved numerically. The model predicts the temporal evolution of an eruption given only its initial conditions and material parameters. Key parameters include magma chamber volume, V_0, initial chamber pressure, chamber aspect ratio, chamber top depth, water and carbon dioxide concentrations, and frictional parameters.

A sample calculation is illustrated in Figure 6. During the eruption the pressure decreases, causing gas to exsolve, increasing the bubble volume fraction, and decreasing the density and dissolved water content. The latter causes the viscosity to increase. The flow velocity monotonically decays as the eruption proceeds and the pressure in the magma chamber diminishes. In this calculation, the eruption is forced to end after 4 years, after which the pressure, density and dissolved water content slightly increase. This system of equations does not exhibit oscillatory behaviour and is, therefore, not appropriate for describing episodic extrusion of the sort observed at some volcanoes (Voight *et al.* 1999; Anderson *et al.* 2010). It does, however, capture the longer-term evolution of extruded volume observed during many effusive eruptions (Anderson & Segall 2011). An advantage of the simplified physical description is that the governing equations integrate very quickly, allowing for Monte Carlo simulations.

The forward model of Anderson & Segall (2011) has been employed in an inversion to constrain properties of the magmatic system at Mount St Helens during the 2004–2008 dome-forming eruption (Anderson & Segall 2013). The data consist of GPS time series, as well as the erupted volume as a function of time. The parameters to be estimated are physical properties, such as the magma chamber volume, depth and aspect ratio, frictional properties, as well as initial conditions, including the initial magma pressure and volatile content. The goal is to estimate the full posterior probability density function (pdf) of the model parameters, which in a Bayesian formulation depends on the *a priori* pdf of these parameters, and the likelihood function, dependent on the goodness of fit to the data. Since the forward model is nonlinear, it is not possible to express the posterior pdf analytically. Rather, we sample the posterior using well-known Markov Chain Monte Carlo (MCMC) methods. Each MCMC step consists of choosing a set of model parameters and comparing model-based predictions to the observations. Models are accepted or rejected according to the Metropolis–Hastings rule (Metropolis *et al.* 1953; Hastings 1970), which always accepts models that fit better than the prior iteration, and randomly accepts models that do not fit as well. The latter prevents the estimation from becoming trapped in local minima. Because the forward calculation is very fast, we are able to compute millions of MCMC iterations, and build up approximations to the posterior pdf.

Anderson & Segall (2013) compare estimations based on standard kinematic models, equivalent deformation models coupled to the analytical eruption results (Equations 8 and 9) and full numerical simulation. The kinematic inversion, employing only the cumulative GPS displacements, resolves the magma chamber depth and aspect ratio. As expected from Equation (1), the kinematic inversion can only determine the product of the chamber volume and pressure change. Inversions based on Equations (8) and (9) fitting the full GPS and extrusion time series are, in addition, able to constrain the system compressibility (through Equation 11).

The numerical physics-based model constrains additional parameters that are either unconstrained

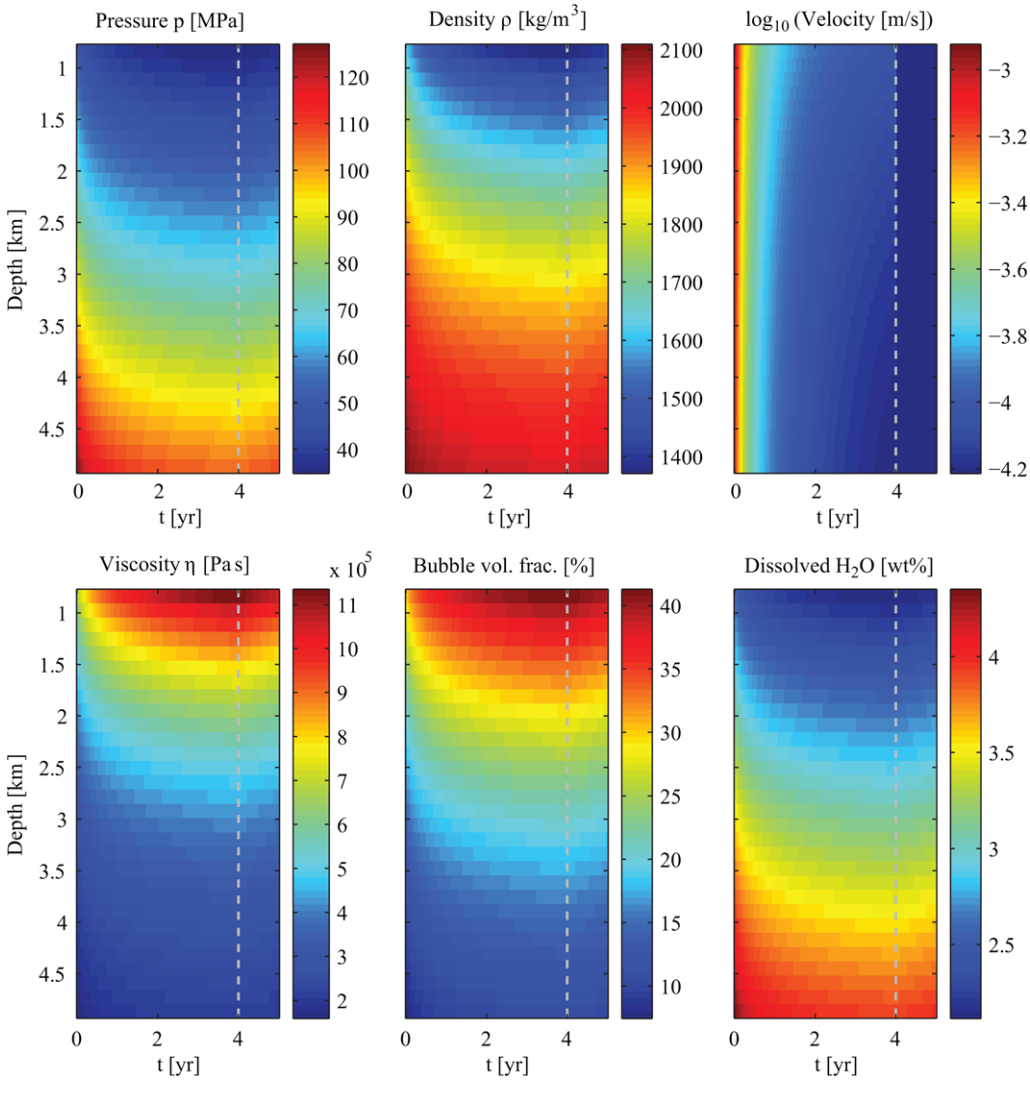

Fig. 6. Evolution of key physical properties during eruption (pressure, density, vertical flow velocity, viscosity, bubble volume fraction and dissolved water content) as a function of depth and time. The eruption is forced to cease after 4 years, vertical dashed line. From Anderson & Segall (2011).

or not even included in simple kinematic inversions (Fig. 7). As in traditional geodetic inversions, the GPS data constrain the (centroid) depth of the magma chamber, and its aspect ratio, as well as the volume change during the eruption. The conduit length, equal to the depth to the top of the magma chamber, and the length of the frictional plug are also reasonably well resolved. In part through *a priori* constraints on overpressure, and the correlations between various parameters, the physics-based model places some constraint on absolute chamber volume and pressure change. The physics-based model is also able to place reasonable constraints on the initial volatile content of the magma, primarily through the influence of exsolved volatiles on compressibility. We find that the data collected during the 2004–2008 eruption do not require recharge into the magma chamber. The large difference between extruded volume (*c.* 100×10^6 m^3) and estimated volume change in the chamber ($<40 \times 10^6$ m^3) can be explained by compressibility effects alone (see also Woods & Huppert 2003; Rivalta & Segall 2008). The physics-based model fits the extrusion data very well, and

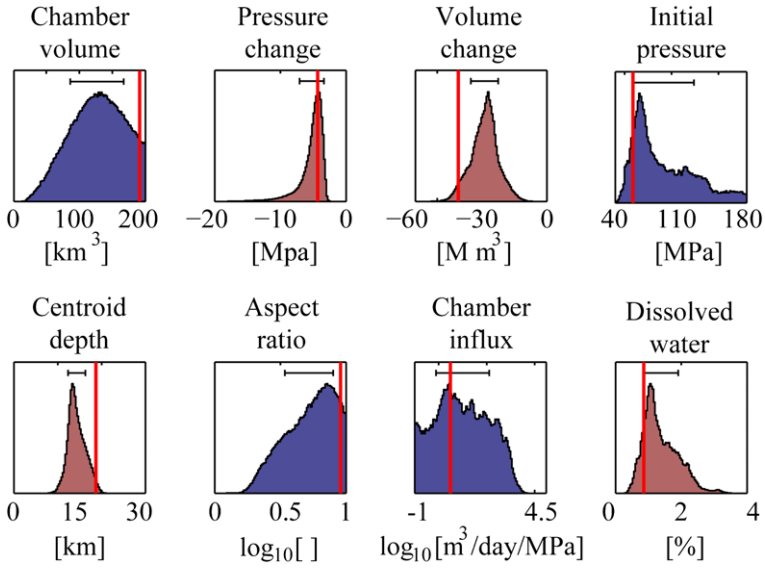

Fig. 7. Marginal distributions for parameters estimated using a physics-based forward model for 2004–2008 eruption of Mount St Helens. Dark grey histograms (blue in online version) are for parameters directly estimated by MCMC inversion, while the lighter grey histograms (salmon-coloured in online version) are dependent parameters. The vertical line (red in online version) is the best-fitting model and the horizontal bar encloses 68% of the distribution. After Anderson & Segall (2013).

the GPS data reasonably well (Fig. 8), given the uncertainties in correcting for tectonic effects in the data (Anderson & Segall 2013).

Eruption forecasting

There have been a number of successful eruption forecasts and even detailed predictions, giving the expected time, location and magnitude of a subsequent eruption. In the next subsection, I briefly review a few case histories, which are notable for various reasons. The following subsection examines the possibility of using reinflation following a past eruption as a measure of likelihood of a subsequent event. The final sections explore two different approaches that I believe offer the potential for significant advance in eruption forecasting. The first explores quantitative integration of deformation and seismicity for imaging dyke propagation. The second explores model-based forecasts conditioned on estimates of material parameters and initial conditions from MCMC inversion of multiple datasets, as discussed in the previous subsection 'More realistic physics and Monte Carlo inversion'.

Selected case histories

St Helens 1980. Remarkably accurate predictions of a series of dome-forming eruptions were made at Mount St Helens, following the catastrophic 18 May 1980 eruption. The predictions were based on a combination of seismic and deformation measurements. Between April 1981 and December 1982, all of seven eruptions were predicted with no false alarms (Malone *et al.* 1983; Swanson *et al.* 1983). Longer-term precursory signals, days to weeks before the eruption, consisted of borehole tilt changes and deformations of the crater floor and dome, particularly motion on thrust faults within the dome and the opening of radial cracks on the crater floor. Shorter-term forecasts were based on dramatic increases in the rate of shallow seismicity.

The remarkably repeatable deformation and seismicity patterns allowed for amazingly precise predictions. Translating those patterns to other volcanoes, however, is far from straightforward, particularly at volcanoes not experiencing repeating dome-forming eruptions. Swanson *et al.* (1983) also noted that predictions of this sort are rarely possible for andesitic and dacitic volcanoes that become active following long periods of quiescence. Furthermore, the deformation monitoring required scientists to be in the active crater, putting themselves at considerable risk. The need for remotely sensed observations was, and remains, clear.

Pinatubo. In terms of societal impact, the forecast of the 1991 eruption of Mount Pinatubo is arguably the greatest success story in volcanology. It has been estimated that tens of thousands of lives were saved, and a major US military installation was

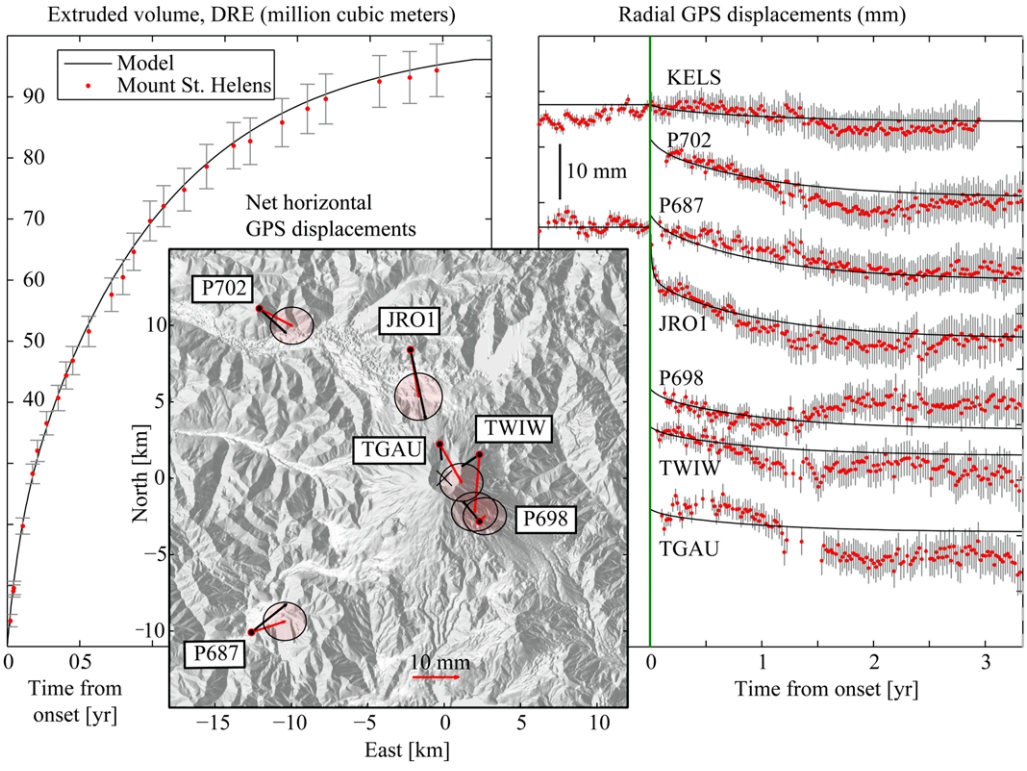

Fig. 8. Fit to the Mount St Helens 2004–2008 data using the physics-based model. (Left) Extruded dome volume (dense rock equivalent) with 1σ error bars. (Right) Radial component of GPS displacements after correcting for tectonic deformation. (Inset) Vector plot of co-eruptive displacements, observed (red with error ellipses) and predicted (black). After Anderson & Segall (2013).

evacuated prior to the eruption. The forecasts were based largely on seismic data, combined with visual observations and reconnaissance mapping that revealed voluminous ash flow sheets surrounding the volcano (Newhall & Punongbayan 1996). Deformation played only a minor role, in part due to the loss of tiltmeters during early phases of the eruption. Deep long-period (LP) earthquakes were recorded in early June 1991; by the second week of June, earthquake activity intensified and concentrated beneath the volcano; significant volcanic tremor occurred and a lava dome appeared. Major 'throat-clearing' eruptions occurred on 12–14 June, accompanied by a 'profound build-up' of LP events. Seismic energy continued to build until the climactic 15 June eruption.

Soufrière Hills Volcano. A remarkable sequence of cyclic tilt events associated with variations in seismic activity were observed by a tiltmeter installed close to the eruptive vent of Soufrière Hills Volcano, Montserrat (Voight *et al.* 1998, 1999). Periodic tilt events, with an amplitude of roughly 10–15 μrad, and periods ranging from 6 to 36 h were observed during May 1997.

The onset of the inflationary part of the cycle was associated with shallow hybrid earthquakes. The hybrid events increased during inflation, diminishing near the peak inflation. High RSAM (Real-Time Seismic-Amplitude Measurement) levels, associated with rockfall and pyroclastic flows, occurred during the deflationary phases. These observations were interpreted as indicating more rapid extrusion during the deflationary phases. Gas measurements showed time-variable SO_2 emissions corresponding to variations in RSAM.

In June 1997, amplitudes of the tilt events increased to roughly 30 μrad, with periods ranging from 8 to 12 h. On 24–25 June, a major deflation event was associated with a large pyroclastic flow, with a volume of 8×10^6 m^3. By August of that year, Soufrière Hills experienced a sequence of volcanian explosions associated with high RSAM and significant deflation (Fig. 9). Before the tiltmeters were destroyed on 5 August by an explosion, the combination of tilt and seismic data proved

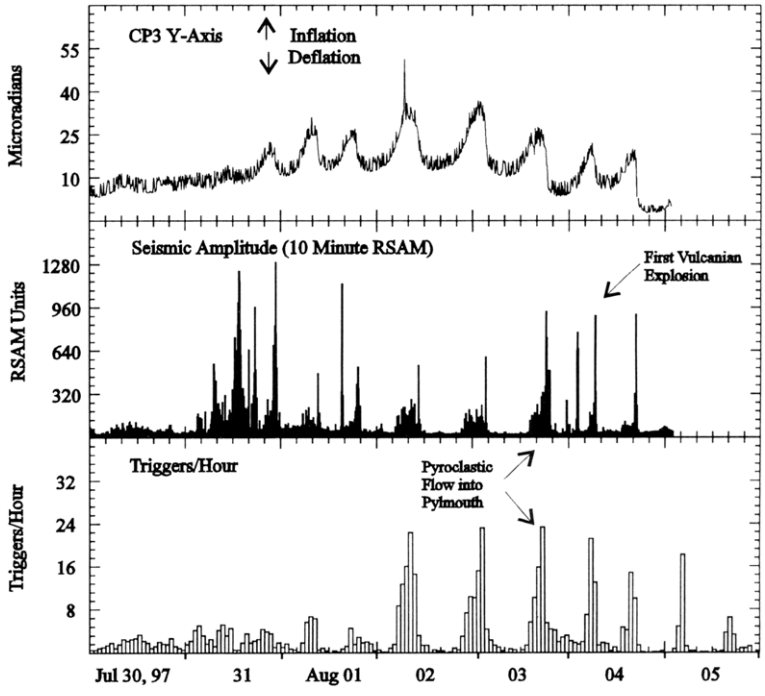

Fig. 9. Tilt, seismic amplitude (RSAM) and earthquake rate during 30 July–5 August 1997 at Soufriere Hill volcano. After Voight *et al.* (1998).

useful in warning of dome collapse events and explosions.

Hekla, 2000. The 2000 eruption of Hekla was arguably the most remarkable short-term volcano forecast ever delivered. The previous eruption of Hekla in 1991 had been preceded by a swarm of shallow earthquakes beneath the volcano, starting roughly 30 min prior to the eruption, as well as strain changes on a borehole dilatometer located 15 km from the volcano summit (Linde *et al.* 1993). A nearly identical pattern was repeated on 26 February, 2000. The description here is based on http://hraun.vedur.is/ja/englishweb/heklanews.html and Soosalu *et al.* (2005).

The first micro-earthquakes near Hekla were recorded at 16:55 on 26 February 2000; volcanic tremor was recorded at about 17:20. At around this time, the Icelandic scientific community was notified of activity that might signal an impending eruption. M 1–2 earthquakes located 1–2 km SE of Hekla's summit were recorded at 17:30, 17:45, 18:17 and 18:26. At 17:31, an automated alert system gave the highest alert for the Hekla region. The National Civil Defence of Iceland was notified at 17:38 that the probability of an eruption in Hekla was high. At 17:47, the BUR strainmeter exhibited a transient very similar to that associated with the 1991 eruption. Based on the 1991 sequence, it was recognized that an eruption could occur within 20–30 min, and the National Civil Defence and Civil Aviation Administration were notified. A change in strain was at 18:17 was interpreted as marking the onset of the eruption; the first eyewitness reports 'were made in the following minutes'. Radar images of the eruption plume were reported at 18:20.

Some of these predictions (Hekla, St Helens and Soufrière Hills Volcano) were remarkable in terms of their precision. The Pinatubo forecast, while less precise, was remarkable in the number of people evacuated and the consequent mitigation of hazard. All four cases were based largely on pattern recognition. At the Mount St Helens and Soufrière Hills volcanoes, the very repeatable patterns of deformation and seismicity allowed subsequent eruptions of the same type to be predicted. At Hekla, the 2000 eruption followed the script set by the 1991 eruption in amazing detail. The Pinatubo forecast was not based on previous eruptions of that particular volcano, although the geological record suggested infrequent large eruptions. In addition, volcanologists there were able to draw on substantial personal experience at other volcanoes, and the ever-increasing seismic energy

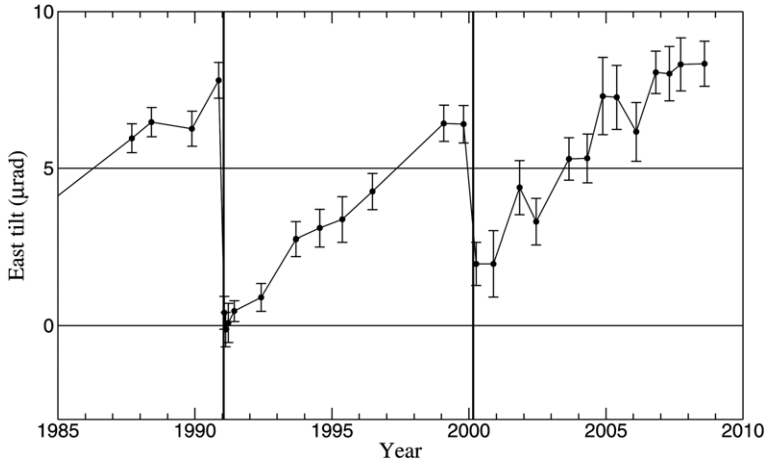

Fig. 10. Tilt at Naefurholt, east of Hekla, from Ofeigsson *et al.* (2011). Vertical lines mark eruptions.

release presented a pattern suggestive of a volcano building to a climactic eruption.

The fact that these successes were based on pattern recognition in no way diminishes these tremendous accomplishments. It does, however, emphasize the question of how to move forward in volcanic settings where the pattern is yet to be established.

Inflation predictable eruptions?

One concept that is widely held is that the next eruption occurs when inflation recovers the deflation accompanying the preceding eruption; I will refer to this as 'inflation predictable', following the 'slip-predictable' concept in earthquake forecasting. Figure 10 shows the tilt record at Hekla Volcano, which lead to the expectation that an eruption would occur by the end of the decade beginning in 2000; at the time of writing, the eruption has yet to occur. A famous water tube tilt record from Krafla (Fig. 11) shows tilt cycles associated with eruptions and intrusions during the fissure swarm of the late 1970s and early 1980s. There was a period during the late 1970s in which the behaviour was crudely inflation predictable; however, the long-term trend was for the tilt threshold to increase with time following the December 1975 deflation. In fact, the 1975 deflation was not recovered until after roughly a dozen subsequent intrusions and eruptions. It is noteworthy that the later deflation events were all associated with eruptions, whereas a majority of the earlier deflation events ended with intrusions.

It is worth considering under what conditions inflation predictability is expected to occur. A related question is how much inflation is required to initiate an intrusion/eruption? At Sierra Negra Volcano, at least 4 m of uplift occurred prior to the 2005 eruption (Fig. 2). However, at Kilauea, and at some of the Iceland volcanoes, uplift between eruptions is typically less than 1 m (Dvorak & Dzurisin 1997).

The stress state in the vicinity of a magma chamber can be written as the sum of a component due to magma chamber inflation and an external stress σ^{∞}:

$$\sigma(x, t) = f\,[p(t), x, t] + \sigma^{\infty}(x, t) \qquad (12)$$

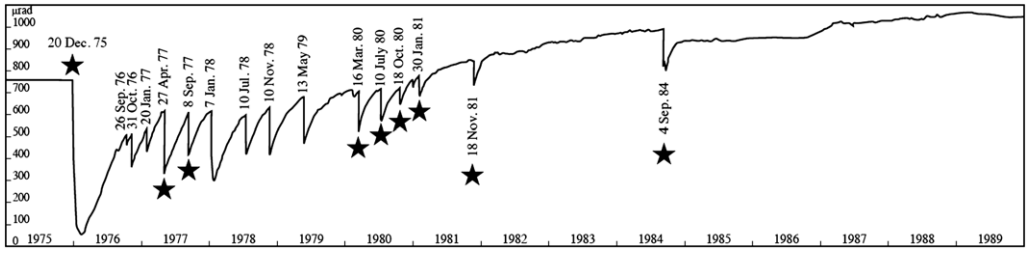

Fig. 11. Water tube tilt record at Krafla power plant. Stars, eruptions. After Sturkell *et al.* (2006).

where $f\,[p(t), x, t]$ indicates that the stress depends on the magma chamber pressure, position x and time t. Consider that the condition for eruption (or intrusion) to be when the stress at the margin of the magma chamber reaches a critical threshold $\sigma(x, t) = \sigma_c$, enabling a dyke to propagate. A more complete description would consider small, magma-filled cracks extending from the chamber walls, such that the critical condition for dyke growth depends on the difference between the magma pressure within the cracks and the compressive stress acting normal to the cracks. However, this only slightly modifies the analysis. Adopting the simpler critical stress condition, the stress relative to the critical threshold is:

$$\begin{aligned}\sigma(x, t) - \sigma_c(x_c, t_c) = {} & f\,[p(t), x, t] \\ & - f\,[p(t_c), x_c, t_c] \\ & + \sigma^\infty(x, t) - \sigma^\infty(x_c, t_c) \quad (13)\end{aligned}$$

where $p(t_c)$ is the pressure at the time of the last event, and t_c, x_c denote the time and position where failure occurred in the last event. Note that for stress below the critical threshold, $\sigma(x, t) - \sigma_c(x_c, t_c) < 0$. If the behaviour of the surroundings is fully elastic, which may be a reasonable assumption if the time between eruptions is short compared to relaxation time of the surrounding crust, then the stress due to inflation is proportional to the magma chamber pressure, $f\,[p(t), x, t] = p(t) f(x)$, so that Equation (13) becomes:

$$\begin{aligned}\sigma(x, t) - \sigma_c(x_c, t_c) = {} & p(t) f(x) - p(t_c) f_c(x_c) \\ & + \sigma^\infty(x, t) - \sigma^\infty(x_c, t_c) \quad (14)\end{aligned}$$

where f_c indicates the stress dependence given the chamber geometry at the time of the last eruption. Assuming that the geometry of the magma chamber and the location on the magma chamber wall where the critical stress is reached remain invariant with time, then $f = f_c$; $x = x_c$. Note that the last assumption might well be violated if the most recent dyke emanated from the point of greatest stress concentration, in part relaxing that stress such that the next dyke starts at a point of lesser stress concentration. If, further, the remote stress and threshold stress remain constant, then:

$$\sigma(x_c, t) - \sigma_c(x_c, t_c) = [p(t) - p(t_c)] f(x_c) \quad (15)$$

and the stress relative to failure is proportional to the change in magma pressure. If, as discussed above, the dyke propagation criterion is more properly the difference between the magma pressure and the compressive stress acting normal to the dyke and the above conditions are all met, Equation (15) would only be modified by changing $f(x_c)$ to $1 + f(x_c)$; the first term giving the direct response to magma pressure, the second giving the change in stress induced by chamber inflation. Something equivalent to Equation (15) also holds, at least under some conditions, for systems in which eruptions result from magma being forced upwards through a pre-existing conduit. One condition is that the conduit is large enough that the opening is insensitive to the applied stress. A second is that the yield strength of the magma and frictional resistance of a solid plug, if present, remain constant. If these conditions are not met then Equation (15) would need to be modified, appropriately.

For elastic deformation the displacement during time interval $t - t_c$ is $u(x, t - t_c) = [p(t) - p(t_c)]\, g(x)$. Here, $u(x, t - t_c)$ includes the deflation during the last eruption, Δu_{defl} and the post-eruptive inflation u_{infl}. Taking this into account and combining with Equation (15) yields:

$$\begin{aligned}\sigma(x_c, t) - \sigma_c(x_c, t_c) = {} & [-\Delta u_{defl}(x) + u_{infl}(x, t - t_c)] \\ & \times f(x_c)/g(x). \quad (16)\end{aligned}$$

Equation (16) is a statement of inflation predictability, namely that the stress relative to the threshold value is proportional to the displacement (or its spatial derivatives) accumulated since the most recent eruption. In summary, threshold predictability requires: (1) elastic deformation; (2) that the geometry of the magma system and the location of failure remain invariant with time; and (3) that the tectonic stress and failure stress remain constant. The conclusion of this analysis comports with expectation; namely, that inflation predictability is not general, but is more likely to hold on shorter timescales when deformation remains elastic and external stresses are less likely to have changed.

Buck *et al.* (2006) modelled the fissure swarm at Krafla, accounting for the fact that each dyke alters the stress field, specifically that dyke intrusions increase the horizontal compressive stress acting normal to the rift zone. In this way, the pressure required to initiate later dykes generally increases, as is inferred from the tilt record (Fig. 11). From Equation (14), we see that if the remote stress decreases (becomes more compressive) with time, $p(t)$ must exceed $p(t_c)$ to reach the threshold condition. The same equation may also explain why volcanoes with active flank spreading (increasing σ^∞), such as Kilauea, generally exhibit lesser amounts of inflation prior to eruption than volcanoes where flank spreading or rifting is not present (e.g. Sierra Negra, Galapagos).

One can also understand the tendency (illustrated in Fig. 11) for later inflation events to end in eruption, as the stress field becomes more compressive with time. There are two critical pressures

required for an eruption to occur: the first is the pressure required to raise a column of magma from depth to (at least very near) the Earth's surface, ρgh, where ρ is magma density. The second is the pressure needed to overcome the dyke normal stress, σ_n, allowing the dyke to dilate. For relatively extensile conditions $\sigma_n < p < \rho gh$ and a dyke might be able to open but not reach the surface. More compressive stress states require greater magma pressure to open the dyke, making it more likely that the pressure can overcome the magmastatic head and allow magma to reach the surface.

Joint analysis of seismicity and deformation

Volcanic eruptions are often preceded by significant seismic activity. It is generally believed that volcano–tectonic (VT) earthquakes are caused by stress changes induced by increasing magma pressure, and/or the propagation of melt through dykes or other conduits. While enhanced levels of seismicity serve as probably the most important precursor to eruptions, we lack a quantitative basis for analysing changes in seismicity along with deformation and other geophysical measurements. For a variety of reasons, swarms of earthquakes accompanying dyke intrusions are a good place to begin investigating this phenomenon.

Migrating swarms of VT earthquakes are commonly associated with dyke intrusions. The 2000 Miyakejima swarm in the Izu islands of Japan included tens of thousands of recorded earthquakes (Sakai *et al.* 2001; Toda *et al.* 2002), some greater than M 6. The swarm of earthquakes on Kilauea Volcano associated with the initiation of the Pu'u O'o eruption propagated down-rift, away from the summit caldera (Rubin *et al.* 1998), and was accompanied by a sequence of tilt changes consistent with a propagating opening dislocation (Okamura *et al.* 1988). In many cases, one can only infer the presence of a dyke; however, in others the onset of fissure eruptions confirms the dyke's location. In one spectacular case, the 1979 Krafla dyke injection was associated with a propagating swarm of earthquakes (Brandsdottir & Einarsson 1979) that breached a geothermal borehole, erupting several cubic metres of basalt tephra (Larsen *et al.* 1979) and so unambiguously tying the dyke to a particular space–time location entirely consistent with the swarm earthquakes.

In order to relate seismicity to other deformation processes we must be able to quantitatively relate changes in stress to changes in seismicity. For VT earthquakes, the seismicity–rate theory of Dieterich (1994) provides such a linkage. The theory is based on current understanding of earthquake nucleation, constrained by laboratory friction studies. An underlying assumption is that at a constant rate of stress increase (i.e. in the absence of stress perturbations), earthquakes occur at a constant rate. If the stressing rate changes, potential earthquake nucleation sites are brought closer to or further from failure, altering the nucleation rate. This theory says nothing about the ultimate size of earthquakes once they initiate; such an analysis would require either specific or statistical information on the spatial distribution of strength and material properties.

The theory relates the seismicity rate $R \equiv \mathrm{d}N/\mathrm{d}t$, where N is the number of earthquakes per unit time, to the stress changes via a state parameter γ:

$$R \equiv \frac{\mathrm{d}N}{\mathrm{d}t} = \frac{r}{\gamma \dot{\tau}_r} \tag{17}$$

$$\frac{\mathrm{d}\gamma}{\mathrm{d}t} = \frac{1}{a\sigma}\left(1 - \gamma\frac{\mathrm{d}s}{\mathrm{d}t}\right) \tag{18}$$

(Dieterich 1994) where r is the background seismicity rate at stressing rate $\dot{\tau}_r$, σ is the normal stress acting on the fault, a is a frictional constitutive parameter and s is the Coulomb stress, $s = \tau - f\sigma$, where τ is shear stress and $f = \tau/\sigma$ is the friction coefficient. Dieterich (1994) also included an indirect effect of normal stress evolution on friction, which we omit here for simplicity, although the form of what follows does not change, simply the definition of s. At the background stressing rate prior to dyke propagation, $\gamma_0 = 1/\dot{\tau}_r$, where we assume for simplicity that the background stressing results solely from changes in shear stress.

The theory does not address the magnitude of the earthquakes, only their occurrence. As a practical matter, the seismicity rates thus refer to a specified magnitude threshold, which must be the same for both R and r. Given the typical size distribution of earthquakes, the seismicity rate will be dominated by events at the completion threshold of the catalogue.

One can approximate any stressing history in terms of piece-wise linear segments, such that the stress rate is piece-wise constant (Segall & Yun 2005; Llenos *et al.* 2011). Under such conditions, Equation (18) can be integrated exactly to obtain an expression relating the seismicity state variable at time step k, γ_k, to the stressing rate, $\dot{s}_k$, during that time step:

$$\gamma_k(t) = \left(\gamma_{k-1} - \frac{1}{\dot{s}_k}\right)\exp\left[\frac{-\dot{s}_k\,(t - t_{k-1})}{a\sigma}\right] + \frac{1}{\dot{s}_k}$$
$$t_{k-1} \le t \le t_k. \tag{19}$$

The stress rate depends on location x relative to the dyke, and time t. Combining Equation (19)

with Equation (17) and integrating yields N, the cumulative number of triggered events, which can be written symbolically as:

$$N(x,t) = r\frac{a\sigma}{\dot{\tau}_\tau}\left\{\sum_{j=1}^{k-1} f\left[\dot{s}_j(x)(t_j - t_{j-1}); \gamma_{j-1}\,\dot{s}_k(x)\right] + f\left[\dot{s}_k(x)(t - t_{k-1}); \gamma_{k-1}\,\dot{s}_k(x)\right]\right\} \quad (20)$$

for t in the interval $t_{k-1} \le t \le t_k$. Note that $t_a \equiv a\sigma/\dot{\tau}_r$ has units of time, and can be interpreted as the characteristic time for earthquakes (aftershocks) to decay to background level following a step change in stress (Dieterich 1994). Note further, that the spatial variation in earthquake activity arises because $\dot{s}_j$ is a function of x. The stress change is, of course, a function of the geometry of the dyke and excess pressure (over the dyke normal stress), Δp, acting within the dyke. For the sake of simplicity, assume that the dyke can be parameterized solely by its length $L_k \equiv L(t_k)$ and excess pressure $\Delta p_k \equiv \Delta p(t_k)$. The dyke-induced stress change is thus of the form $\Delta s(x,t) = \Delta p(t) g(L,x)$, where $g(L,x)$ is a function of dyke geometry. A finite-difference approximation to the stress-rate is thus:

$$\dot{s}_k(x) \approx \frac{\Delta p(t_k) g(L_k, x) - \Delta p(t_{k-1}) g(L_{k-1}, x)}{t_k - t_{k-1}}. \quad (21)$$

The number of triggered earthquakes can, thus, be computed by introducing Equation (21) into Equation (20).

Figure 12 shows the predicted seismicity in response to a propagating dyke for two points: one below the bottom edge of the dyke; and, the second, adjacent to the dyke. In this calculation, earthquakes were assumed to occur on optimally orientated strike-slip faults. The point below the dyke experiences an increasing stress as the dyke propagates towards it, while the stress levels off after the dyke tip passes. This leads to first an increasing stress rate followed by a decreasing stress rate. The seismicity rate, $R(t)$, thus increases to a maximum and then gradually decays to background, with time constant controlled by t_a. In contrast, the point adjacent to the dyke experiences a similar increase in stress, but then falls into a 'stress shadow' once the dyke tip passes. This causes the stress rate to become negative, resulting in a very abrupt decrease in the seismicity rate. The maximum seismicity rate is sensitive to $\dot{\tau}_r$ and t_a, while the time to decay to background scales

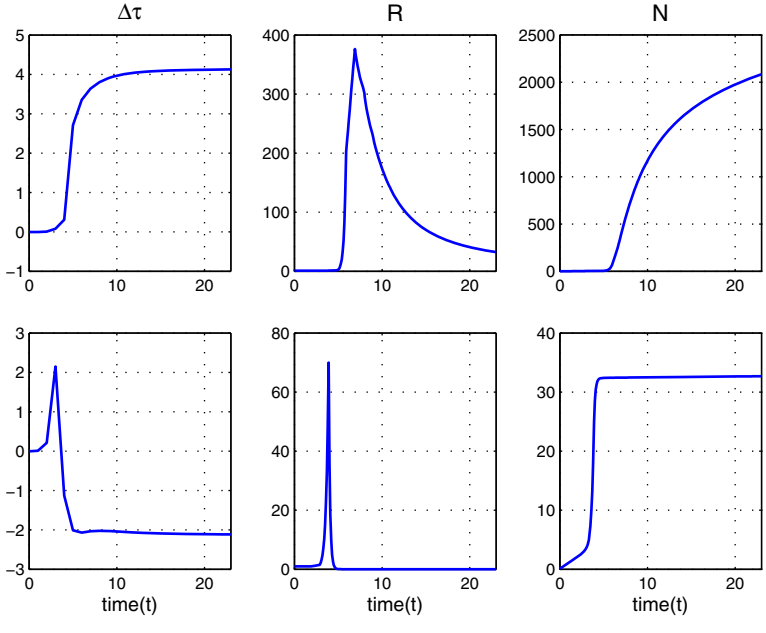

Fig. 12. Coulomb stress change due to propagating dyke, $\Delta\tau$, seismicity rate, R, and cumulative number of events, N, as a function of time for two points near the dyke plane. (Top row) A point below the bottom edge of the dyke. (Bottom row) A point adjacent to the dyke. After Segall & Yun (2005).

with t_a, so that these parameters can, in principle, be estimated from the seismicity data.

Given a forward model for changes in seismicity rate, it is possible to jointly analyse deformation data, d, and seismic observations. Deformation data is a non-linear function of dyke geometry, but linear in excess pressure, thus $d(t) = \Delta p(t)\tilde{g}[L(t)]$, where $\tilde{g}[L(t)]$ also depends on dyke geometry. This can be combined with Equation (20) in an optimization scheme to determine L_k, Δp_k, as well as the parameters $a\sigma$, $\dot{\tau}_r$ (or t_a) by minimizingan objective function of the form $\Phi = \sum_j (\|\Sigma^{-1/2}(d_j - \hat{d}_j)\|^2 + \kappa^2 \|N_j - \hat{N}_j\|^2)$. Here, the notation $\hat{}$ indicates predicted value, Σ is the deformation data covariance matrix, κ^2 is a scalar that weights fitting the seismicity relative to the geodetic data and the sum on j adds the misfit in all time epochs.

A numerical test using simulated seismicity and deformation data is shown in Figure 13. A model dyke propagates unilaterally at variable speed and then stops. The dyke excess pressure initially declines as the dyke extends, and then very slightly recovers after propagation ceases. In this example, noise was added equivalent to 20% of the signal for both deformation (four GPS stations and one tiltmeter) and seismicity data. The location of the fixed dyke end and the azimuth of propagation, as well as the depth extent of the dyke opening were fixed to the true values. The stressing rate in Equation (21) depends on the orientation of the faults with respect to the dyke, as well as on the friction coefficient, f. Strike-slip faulting is assumed. For the forward run, the right-lateral plane was used with $f = 0.6$, whereas for the inversion the conjugate plane was assumed with $f = 0.4$ (note that the stresses off the dyke are not symmetric with respect to the conjugate planes). Inversions, based on the method outlined above, are able to recover the true pressure and dyke length histories reasonably well (Fig. 13). In addition, the estimates of $a \approx 0.006$ and $\dot{\tau}_r \approx 2.3 \times 10^{-5}$ MPa/h, are acceptably close to the input values of $a = 0.01$ and $\dot{\tau}_r = 3 \times 10^{-5}$ MPa/h. Of course, the assumptions that go into the forward model are the same as those used in the inversion, and these assumptions may not be met in nature. Testing of the approach on well-recorded intrusions will be necessary to confirm or refute these assumptions.

Physics-based forecasts

The air traffic disruption resulting from the 2010 Eyjafjallajökull eruption focused attention on the volcanological community's ability to forecast the duration and ultimate size of an ongoing eruption. Important information came from the durations of previous eruptions of this volcano (Gudmundsson *et al.* 2010). The financial losses associated with the eruption, however, motivates improvement of

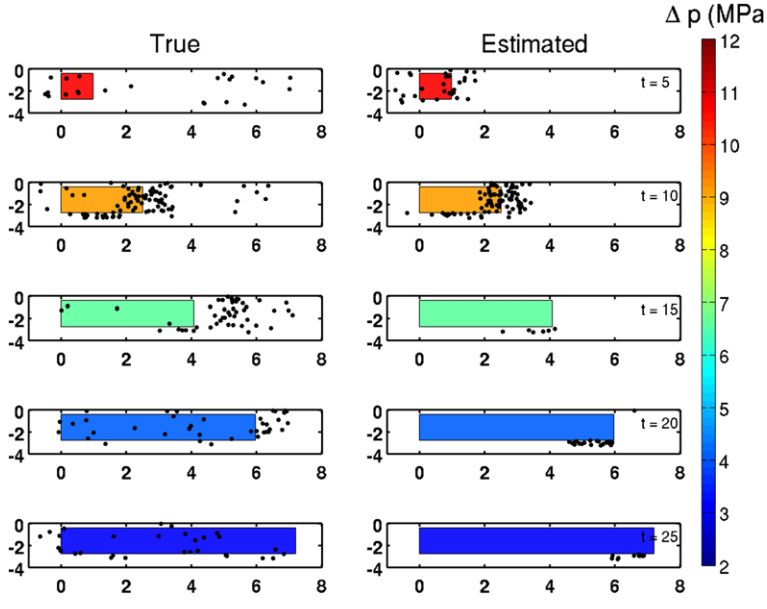

Fig. 13. Simulation of the joint deformation–seismicity inversion. A comparison of the true model (left) with the inversion results (right), showing 2 h time snapshots of the dyke length in each row. Colours indicate the excess magma pressure, Δp, at each time snapshot. Dots indicate seismicity triggered by the intrusion. After Llenos *et al.* (2011).

estimates regarding the duration of the eruption from a combination of measurements and physical models. For example, measurements of magma chamber deflation are sensitive to the decrease in pressure within the magma chamber, and thus place some constraints on the pressure available to drive continued effusion.

Scientists at the Cascades Volcano Observatory did attempt to forecast the duration and final extruded volume of the 2004–2008 dome-forming eruption of Mount St Helens (Mastin *et al.* 2009). These authors fitted the extruded volume as a function of time to analytical models (analogous to Equation 9), using data available at various times during the eruption (Fig. 14). They found that given data up to 440 days after the eruption onset (or less) it was not possible to distinguish between scenarios with no recharge, which asymptotically approach a final volume, from scenarios with recharge, which approach a steady-state eruption. By 750 days (*c.* 2 years) after eruption onset, the model with no recharge fits somewhat better than one with recharge. By this date, the estimated total erupted volume, assuming no influx, is close to the ultimate value (Fig. 14). Limitations in this approach are: first, that it can be difficult to get meaningful uncertainties in the forecasts; and, second, that it may be difficult to extend to more realistic models for which analytical solutions are lacking.

We can extend physics-based forecasts to more complex eruption models, including temporal variations in physical properties (density, viscosity, etc.) using the Monte Carlo inversion procedure described above and in Anderson & Segall (2013). A simple test of this was conducted using the same dome extrusion data employed by Mastin *et al.* (2009), but also including the corresponding GPS time series. The procedure was to take data (both erupted volume and GPS) only up to a fixed time after the eruption onset, and estimate initial conditions and material parameters using the Markov Chain Monte Carlo (MCMC) procedure discussed above. This yields sets of model parameters consistent with the available data. Because the underlying physical model is fully deterministic, it can be used to predict future behaviour once the initial conditions and material properties are specified. We next take a random subset of the accepted model parameters and forecast the erupted volume as a function of time. The results of one such analysis are shown in Figure 15, which included data up to 2 years after the start of the eruption. While the GPS data is not shown, it was included in the model estimation step. The

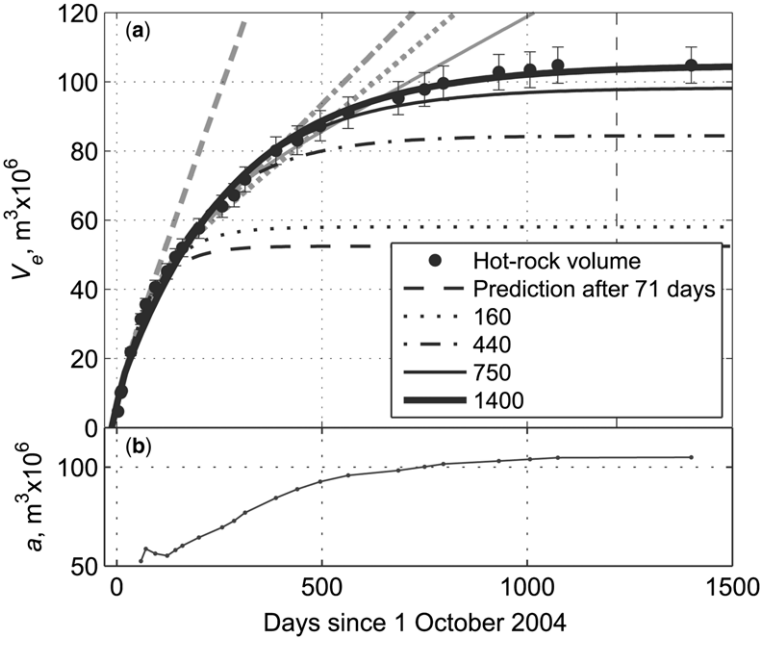

Fig. 14. (**a**) Comparison of erupted volume (points with error bars) with model forecasts at Mount St Helens using data up to a specified number of days (shown in key). Model with constant recharge shown in light lines; no recharge darker line. (**b**) Estimated final erupted volume as a function of time of forecast assuming no recharge. Figure from Mastin *et al.* (2009).

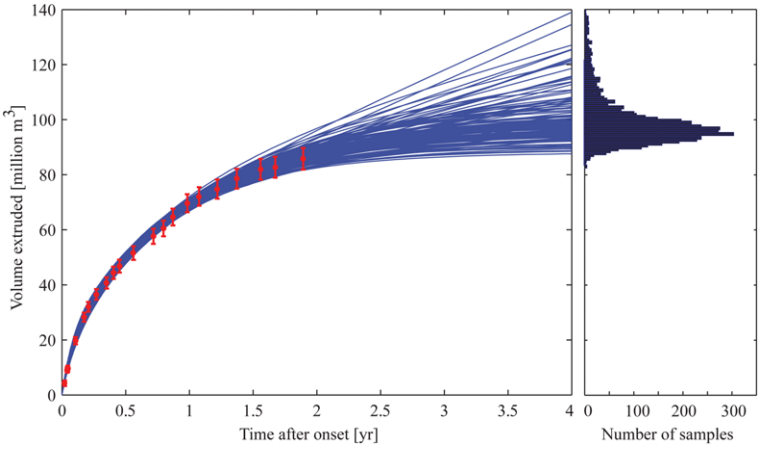

Fig. 15. Example of MCMC forecast using data from Mount St Helens for 2 years following eruption onset. Extruded volume is shown with 1σ error bars (red in online version). MCMC procedure yields a large set of model estimates consistent with the data (GPS data not shown). The model parameters were then used to simulate the erupted volume as a function of time (curves; 150 trajectories are shown). Right panel shows total erupted volume at the end of 4 years (5000 samples).

blue curves illustrate the projected trajectories of the extruded volume as a function of time. The spread in the trajectories increases with time past the available data, as the prediction necessarily becomes less precise with time. In particular, some models predict no recharge such that the trajectories asymptotically approach a fixed final volume, while others include recharge and approach steady effusion. A histogram of total erupted volume at the end of 4 years is shown on the right-hand side in Figure 15.

Recall that this forward model is only valid for effusive eruptions, and does not include cooling, crystallization or other processes that would cause the eruption to terminate before the pressure drops to magmastatic. Thus, this simple version cannot predict the end of the eruption. However, the estimated volume 3.5 years after the onset of the eruption agrees reasonably well with the observed value (*c*. 100×10^6 m^3).

The physics-based MCMC forecast approach has substantial advantages. First of all, the forecast is based on all knowledge of the system, including data up to the current date. The underlying model is completely deterministic; however, because the method samples initial conditions and physical parameters consistent with the given data, it yields probabilistic forecasts including uncertainties in the underlying parameters.

This forecasting approach can be extended to forward models beyond those considered here, including those appropriate for explosive eruptions. It should, however, be recognized that uncertainties associated with processes not included in the physical model will not be captured by the MCMC forecast approach. These are so-called *epistemic uncertainties*, which are separate from the uncertainty associated with noisy measurements. For example, a physics-based model including a single magma chamber cannot faithfully predict the range of outcomes associate with, for example, a dyke intersecting a second magma reservoir. The apparent mixing of two different magma types at Eyjafjallajökull is an example of this phenomenon (Sigmundsson *et al.* 2010). Another example might be the failure to account for changes in the conduit geometry with time. Pressure-dependent transmissivity may lead to non-linear response in which the influx is pulse-like rather than steady. Nevertheless, I would suggest that the very process of attempting to build deterministic forecast models will prove to be instructive, and that lessons learned from failures could be incorporated into future models. There is, therefore, likely to be a substantial learning curve as models evolve to become more realistic.

Summary

Deformation measurements alone place limited constraints on subsurface magma reservoirs and flow. The challenge for deterministic forecasting is how to combine these data with seismic, gas emission and other observations, as well as with quantitative models of the underlying physical and chemical processes. I have suggested two areas with potential for substantial progress. The first is relating seismicity rate changes to changes in

stress associated with dyke intrusions. This gives the potential for improved imaging of dyke propagation through combined seismic and geodetic monitoring. It remains to be seen whether this approach yields improved eruption forecasts, given sufficiently dense real-time seismic and geodetic monitoring.

A second area that offers promise is physics-based MCMC forecasting of an ongoing eruption. By combining deformation and effusion data with physical eruption models, it should, in principle, be possible to forecast the duration of an eruption and the final erupted volume. Again, much work remains to be done; however, the MCMC-forecast approach combines probabilistic forecasting with underlying deterministic models. It also offers a framework for combining multiple observation types in a single forecast.

I would like to thank the meeting organizers, D. Pyle, T. Mather and J. Biggs, for inviting me to give the 2011 William Smith Lecture of the Geological Society of London, which formed the basis for this review. I would also like to thank K. Anderson, A. Llenos, and S.-H. Yun for assistance in preparing the paper, M. Poland and F. Sigmundsson for discussion and comments, and L. Mastin and T. Wright for careful reviews.

References

Albino, F., Pinel, V., Massol, H. & Collombet, M. 2011. Conditions for detection of ground deformation induced by conduit flow and evolution. *Journal of Geophysical Research*, **116**, B06201.

Amelung, F., Jónsson, S., Zebker, H. & Segall, P. 2000. Widespread uplift and 'trapdoor' faulting on Galapagos volcanoes observed with radar interferometry. *Nature*, **407**, 993–996.

Anderson, K. & Segall, P. 2011. Physics-based models of ground deformation and extrusion rate at effusively erupting volcanoes. *Journal of Geophysical Research*, **116**, B07204, http://dx.doi.org/10.1029/2010JB007939

Anderson, K. & Segall, P. 2013. Bayesian inversion of data from effusive volcanic eruptions using physics-based models: Application to Mount St. Helens 2004–2008. *Journal of Geophysical Research*, in press.

Anderson, K., Lisowski, M. & Segall, P. 2010. Cyclic ground tilt associated with the 2004–2008 eruption of Mount St. Helens. *Journal of Geophysical Research*, **115**, http://dx.doi.org/10.1029/2009JB007102.

Brandsdottir, B. & Einarsson, P. 1979. Seismic activity associated with the September 1977 deflation of the Krafla central volcano in northern Iceland. *Journal of Volcanology*, **6**, 197–212.

Buck, W. R., Einarsson, P. & Brandsdottir, B. 2006. Tectonic stress and magma chamber size as controls on dike propagation: constraints from the 1975–1984 Krafla rifting episode. *Journal of Geophysical Research*, **111**, B12404, http://dx.doi.org/10.1029/2005JB003879

Chadwick, W., Geist, D., Jónsson, S., Poland, M., Johnson, D. & Meertens, C. 2006. A volcano bursting at the seams: inflation, faulting, and eruption at Sierra Negra volcano, Galápagos. *Geology*, **34**, 1025–1028.

Collier, L. & Neuberg, J. 2006. Incorporating seismic observations into 2D conduit flow modeling. *Journal of Volcanology and Geothermal Research*, **152**, 331–346, http://dx.doi.org/10.1016/j.jvolgeores.2005.11.009

Collombet, M. 2009. Two-dimensional gas loss for silicic magma flows: toward more realistic numerical models. *Geophysical Journal International*, **177**, 309–318.

Dieterich, J. 1994. A constitutive law for rate of earthquake production and its application to earthquake clustering. *Journal of Geophysical Research – Solid Earth*, **99**, 2601–2618.

Dieterich, J. H. & Decker, R. W. 1975. Finite element modeling of surface deformation associated with volcanism. *Journal of Geophysical Research*, **80**, 4094–4102, http://dx.doi.org/10.1029/JB080i029p04094

Dobran, F. 2001. *Volcanic Processes: Mechanisms in Material Transport*. Plenum, New York.

Dvorak, J. J. & Dzurisin, D. 1997. Volcano geodesy: the search for magma reservoirs and the formation of eruptive vents. *Reviews of Geophysics*, **35**, 343–384.

Ebinger, C., Ayele, A. *et al.* 2010. Length and timescales of rift faulting and magma intrusion: the afar rifting cycle from 2005 to present. *Annual Review of Earth and Planetary Sciences*, **38**, 439–466, http://dx.doi.org/10.1146/annurev-earth-040809-152333

Geist, D. J., Harpp, K. S., Naumann, T. R., Poland, M., Chadwick, W. W., Hall, M. & Rader, E. 2008. The 2005 eruption of Sierra Negra volcano, Galapagos, Ecuador. *Bulletin of Volcanology*, **70**, 655–673, http://dx.doi.org/10.1007/s00445-007-0160-3

Grandin, R., Socquet, A. *et al.* 2009. September 2005 Manda Hararo-Dabbahu rifting event, afar (Ethiopia): constraints provided by geodetic data. *Journal of Geophysical Research*, **114**, B08404, http://dx.doi.org/10.1029/2008JB005843

Gudmundsson, M. T., Pedersen, R., Vogfjörd, K., Thorbjarnardóttir, B., Jakobsdóttir, S. & Roberts, M. J. 2010. Eruptions of Eyjafjallajökull volcano, Iceland. *Eos, Transactions of the American Geophysical Union*, **91**, 190.

Hastings, W. K. 1970. Monte Carlo sampling methods using Markov chains and their applications. *Biometrika*, **57**, 97–109, http://biomet.oxfordjournals.org/cgi/content/abstract/57/1/97

Huppert, H. E. & Woods, A. W. 2002. The role of volatiles in magma chamber dynamics. *Nature*, **420**, 493–495, http://dx.doi.org/10.1038/nature01211

Jaupart, C. & Tait, S. 1990. Dynamics of eruptive phenomena. *In*: Nicholls, J., Russell, J. K. & Ribbe, P. H. (eds) *Modern Methods of Igneous Petrology: Understanding Magmatic Processes*. Mineralogical Society of America, Reviews in Mineralogy, **24**, 213–238.

Jónsson, S., Zebker, H. & Amelung, F. 2005. On trapdoor faulting at Sierra Negra volcano, Galápagos.

Journal of Volcanology and Geothermal Research, **144**, 59–71.

Kozono, T. & Koyaguchi, T. 2009. Effects of relative motion between gas and liquid on 1-dimensional steady flow in silicic volcanic conduits: 1. an analytical method. *Journal of Volcanology and Geothermal Research*, **180**, 21–36.

Larsen, G., Gronvold, K. G. & Thorarinsson, S. 1979. Volcanic eruption through a geothermal borehole at Namafjall, Iceland. *Nature*, **278**, 707–710.

Linde, A. T., Agustsson, K., Sacks, I. S. & Stefansson, R. 1993. Mechanism of the 1991 eruption of Hekla from continuous borehole strain monitoring. *Nature*, **365**, 737–740.

Lisowski, M., Dzurisin, D., Denlinger, R. P. & Iwatsubo, E. Y. 2008. Analysis of GPS-measured deformation associated with the 2004–2006 dome-building eruption of Mount St. Helens, Washington. *In*: Sherrold, D. R., Scott, W. E. & Stauffer, P. H. (eds) *A Volcano Rekindled: The Renewed Eruption of Mount St. Helens, 2004–2006*. US Geological Survey, Professional Papers, **1750**, 281–300.

Llenos, A. L., Segall, P., Thurber, C. H., Syracuse, E. M. & Peterson, D. 2011. Modeling time-dependent dike propagation during the 2007 Father's Day intrusion from seismicity and deformation data. *In*: *American Geophysical Union, Fall Meeting 2011*. American Geophysical Union, Washington, DC, Abstract V22A-06.

Malone, S. D., Boyko, C. & Weaver, C. S. 1983. Seismic precursors to the Mount St. Helens eruptions in 1981 and 1982. *Science*, **221**, 1376–1378, http://www.sciencemag.org/content/221/4618/1376.abstract

Mastin, L. G. & Ghiorso, M. S. 2000. *A Numerical Program for Steady-State Flow of Magma–Gas Mixtures Through Vertical Eruptive Conduits*. US Geological Survey, Open-File Report **00-209**.

Mastin, L. G., Roeloffs, E., Beeler, N. M. & Quick, J. E. 2008. Constraints on the size, overpressure, and volatile content of the Mount St. Helens magma system from geodetic and dome-growth measurements during the 2004–2006 eruption. *In*: Sherrold, D. R., Scott, W. E. & Stauffer, P. H. (eds) *A Volcano Rekindled: The Renewed Eruption of Mount St. Helens, 2004–2006*. US Geological Survey, Professional Papers, **1750**, 461–488.

Mastin, L. G., Lisowski, M., Roeloffs, E. & Beeler, N. 2009. Improved constraints on the estimated size and volatile content of the Mount St. Helens magma system from the 2004–2008 history of dome growth and deformation. *Geophysical Research Letters*, **36**, L20304, http://dx.doi.org/10.1029/2009GL039863

McTigue, D. F. 1987. Elastic stress and deformation near a finite spherical magma body - resolution of the point-source paradox. *Journal of Geophysical Research*, **92**, 12 931–12 940.

Melnik, O. & Sparks, R. S. J. 2005. Controls on conduit magma flow dynamics during lava dome building eruptions. *Journal of Geophysical Research*, **110**, http://dx.doi.org/10.1029/2004JB003183

Metropolis, N., Rosenbluth, A. W., Rosenbluth, M. N., Teller, A. H. & Teller, E. 1953. Equation of state calculations by fast computing machines. *Journal of Chemical Physics*, **21**, 1087–1092.

Mogi, K. 1958. Relations between the eruptions of various volcanoes and the deformations of the ground surfaces around them. *Bulletin of the Earthquake Research Institute University of Tokyo*, **36**, 99–134.

Newhall, C. G. & Punongbayan, R. 1996. *Fire and mud: Eruptions and Lahars of Mount Pinatubo*. Philippine Institute of Volcanology and Seismology, Quezon City, The Philippines.

Nishimura, T. 2009. Ground deformation caused by magma ascent in an open conduit. *Journal of Volcanology and Geothermal Research*, **187**, 178–192, http://dx.doi.org/10.1016/j.jvolgeores.2009.09.001

Ofeigsson, B. G., Hooper, A., Sigmundsson, F., Sturkell, E. & Grapenthin, R. 2011. Deep magma storage at Hekla volcano, Iceland, revealed by InSAR time series analysis. *Journal of Geophysical Research*, **116**, B05401.

Okamura, A., Dvorak, J. J., Koyanagi, R. & Tanigawa, W., 1988. Surface deformation during dike propagation. *In*: Wolfe, E. (ed.) *The Pu'u O'o Eruption of Kilauea Hawaii: Episodes 1 Through 20, January 3, 1983 Through June 8, 1984*. US Geological Survey, Professional Papers, **1463**, 165–182.

Owen, S., Segall, P., Lisowski, M., Miklius, A., Murray, M., Bevis, M. & Foster, J. 2000. January 30, 1997 eruptive event on Kilauea volcano, Hawaii, as monitored by continuous GPS. *Geophysical Research Letters*, **27**, 2757–2760.

Rivalta, E. & Segall, P. 2008. Magma compressibility and the missing source for some dike intrusions. *Geophysical Research Letters*, **35**, L04306, http://dx.doi.org/10.1029/2007GL032521

Rubin, A. M., Gillard, D. & Got, J.-L. 1998. A reinterpretation of seismicity associated with the January 1983 dike intrusion at Kilauea volcano, Hawaii. *Journal of Geophysical Research*, **103**, 10 003–10 015.

Sahagian, D. 2005. Volcanic eruption mechanisms: insights from intercomparison of models of conduit processes. *Journal of Volcanology and Geothermal Research*, **143**, 1–15.

Sakai, S. I., Yamada, T. *et al.* 2001. Magma migration from the point of view of seismic activity in the volcanism of Miyake-Jima Island in 2000. *Journal of Geography*, **110**, 145–155.

Segall, P. 2010. *Earthquake and Volcano deformation*. Princeton University Press, Princeton, NJ.

Segall, P. & Yun, S. H. 2005. Imaging dike intrusion by joint inversion of deformation and seismicity. *In*: *American Geophysical Union, Fall Meeting 2005*. American Geophysical Union, Washington, DC, Abstract V14B-01.

Segall, P., Cervelli, P., Owen, S., Lisowski, M. & Miklius, A. 2001. Constraints on dike propagation from continuous gps measurements. *Journal of Geophysical Research – Solid Earth*, **106**, 19301–19317.

Sigmundsson, F., Hreinsdóttir, S. *et al.* 2010. Intrusion triggering of the 2010 Eyjafjallajokull explosive eruption. *Nature*, **468**, 426–430.

Soosalu, H., Einarsson, P. & Orbjarnardóttir, B. S. 2005. Seismic activity related to the 2000 eruption of the Hekla volcano, Iceland. *Bulletin of Volcanology*, **68**, 21–36.

Sparks, R. S. J. 2003. Forecasting volcanic eruptions. *Earth and Planetary Science Letters*, **210**, 1–15.

Stasiuk, M. V., Jaupart, C. & Sparks, R. S. J. 1993. On the variations of flow-rate in nonexplosive lava eruptions. *Earth and Planetary Science Letters*, **114**, 505–516, http://dx.doi.org/10.1016/0012-821X(93) 90079-O

Sturkell, E., Einarsson, P. *et al*. 2006. Volcano geodesy and magma dynamics in Iceland. *Journal of Volcanology and Geothermal Research*, **150**, 14–34.

Swanson, D. A., Casadevall, T. J., Dzurisin, D., Malone, S. D., Newhall, C. G. & Weaver, C. S. 1983. Predicting eruptions at Mount St. Helens, June 1980 through December 1982. *Science*, **221**, 1369–1376, http://www.sciencemag.org/content/221/4618/1369.abstract

Toda, S., Stein, R. S. & Sagiya, T. 2002. Evidence from the ad 2000 Izu islands earthquake swarm that stressing rate governs seismicity. *Nature*, **419**, 58–61.

Voight, B., Hoblitt, R. P., Clarke, A. B., Lockhart, A. B., Miller, A. D., Lynch, L. & McMahon, J. 1998. Remarkable cyclic ground deformation monitored in real-time on Montserrat, and its use in eruption forecasting. *Geophysical Research Letters*, **25**, 3405–3408.

Voight, B., Sparks, R. S. J. *et al*. 1999. Magma flow instability and cyclic activity at Soufriere Hills Volcano, Montserrat, British West Indies. *Science*, **283**, 1138–1142.

Wilson, L., Sparks, R. S. J. & Walker, G. P. L. 1980. Explosive volcanic eruptions – iv. The control of magma properties and conduit geometry on eruption column behaviour. *Geophysical Journal of the Royal Astronomical Society*, **63**, 117–148.

Woods, A. W. 1995. The dynamics of explosive volcanic eruptions. *Reviews of Geophysics*, **33**, 495–530, http://dx.doi.org/10.1029/95RG02096

Woods, A. W. & Huppert, H. E. 2003. On magma chamber evolution during slow effusive eruptions. *Journal of Geophysical Research*, **108**, 2403, http://dx.doi.org/10.1029/2002JB002019

Wright, T. J., Ebinger, C., Biggs, J., Ayele, A., Yirgu, G., Keir, D. & Stork, A. 2006. Magma-maintained rift segmentation at continental rupture in the 2005 afar Dyking episode. *Nature*, **442**, 291–294, http://dx.doi.org/10.1038/nature04978

Wright, T. J., Sigmundsson, F. *et al*. 2012. Geophysical constraints on the dynamics of spreading centres from rifting episodes on land. *Nature Geoscience*, **5**, 242–250.

Yang, X. M., Davis, P. M. & Dieterich, J. H. 1988. Deformation from inflation of a dipping finite prolate spheroid in an elastic half-space as a model for volcanic stressing. *Journal of Geophysical Research – Solid Earth and Planets*, **93**, 4249–4257.

Yun, S., Segall, P. & Zebker, H. 2006. Constraints on magma chamber geometry at Sierra Negra volcano, Galapagos Islands, based on InSAR observations. *Journal of Volcanology and Geothermal Research*, **150**, 232–243.